Journal of Hazardous Materials 189 (2011) 108–118

Contents lists available at ScienceDirect

Journal of Hazardous Materials

journal homepage: www.elsevier.com/locate/jhazmat

Integrated detoxification methodology of hazardous phenolic wastewaters in environmentally based trickle-bed reactors: Experimental investigation and CFD simulation

Rodrigo J.G. Lopes*, Teresa S.A. Almeida, Rosa M. Quinta-Ferreira

Centro de Investigação em Engenharia dos Processos Químicos e Produtos da Floresta (CIEPQPF), GERSE – Group on Environmental, Reaction and Separation Engineering, Department of Chemical Engineering, University of Coimbra, Rua Sílvio Lima, Polo II – Pinhal de Marrocos, 3030-790 Coimbra, Portugal

ARTICLE INFO

Article history:
Received 16 August 2010
Received in revised form 2 February 2011
Accepted 3 February 2011
Available online 5 March 2011

Keywords:
Hazardous wastewaters
Computational fluid dynamics
Trickle-bed reactor
Multiphase flow
Catalytic wet oxidation
Total organic carbon

ABSTRACT

Centralized environmental regulations require the use of efficient detoxification technologies for the secure disposal of hazardous wastewaters. Guided by federal directives, existing plants need reengineering activities and careful analysis to improve their overall effectiveness and to become environmentally friendly. Here, we illustrate the application of an integrated methodology which encompasses the experimental investigation of catalytic wet air oxidation and CFD simulation of trickle-bed reactors. As long as trickle-bed reactors are determined by the flow environment coupled with chemical kinetics, first, on the optimization of prominent numerical solution parameters, the CFD model was validated with experimental data taken from a trickle bed pilot plant specifically designed for the catalytic wet oxidation of phenolic wastewaters. Second, several experimental and computational runs were carried out under unsteady-state operation to evaluate the dynamic performance addressing the TOC concentration and temperature profiles. CFD computations of total organic carbon conversion were found to agree better with experimental data at lower temperatures. Finally, the comparison of test data with simulation results demonstrated that this integrated framework was able to describe the mineralization of organic matter in trickle beds and the validated consequence model can be exploited to promote cleaner remediation technologies of contaminated waters.

1. Introduction

In the field of environmental reaction engineering, long-established technologies have been intensified during the last decade to demonstrate new potentialities and hindrances from a process viewpoint. Having recognized the effect of technological threats generated by dangerous substances on the environment, it is possible to identify a gap of knowledge on how to provide consistent remediation technologies of contaminated air, soil and water. In this regard, multiphase reactors such as trickle-bed reactors (TBRs) can then be evaluated on further deployment for the catalytic abatement of moderate- to high-strength wastewaters if one takes into account modern and advanced simulation tools as CFD codes.

The specialized literature identified various dynamic circumstances in TBRs as a new breed potential for performance enhancement arising from the interaction between the gas and liquid phases in supplying reactants to the catalyst surface and pores. This fact is even reinforced due to the multifaceted relationship between fluid dynamics, catalyst wetting and chemical reaction. Multiphase reactors such as TBRs have been commonly designed and operated under steady-state mode in the industrial applications. However, novel operating modes under transient conditions have generated an emergent interest in view of the significant performance enhancement encompassing chemical conversion and products selectivity [1–4]. The transient operation of TBR revealed key characteristics reinforced by the dynamic nature of gas–liquid flow over the catalyst packing, which ultimately leads to the cumbersome non-linearity behaviour of trickle beds [5]. Here, we pursue our prior efforts to provide new insights on environmentally based TBRs to detoxify hazardous polluted liquid streams. This task is sought to be accomplished by the experimental work devoted to investigate the suitability of this methodology as well as by state-of-the-art simulation tools considered by CFD codes. The case study encompasses the application of a trickle-bed reactor to the detoxification of phenolic wastewaters through a series of experimental runs accompanied and validated by a multiphase Volume-of-Fluid (VOF) model formerly reported by Lopes and Quinta-Ferreira [6]. At a first glance, a brief prospect of literature on trickle-bed reactor modelling and validation is presented at reaction conditions.

* Corresponding author. Tel.: +351 239798723; fax: +351 239798703.
E-mail address: rodrigo@eq.uc.pt (R.J.G. Lopes).

0304-3894/$ – see front matter © 2011 Elsevier B.V. All rights reserved.
doi:10.1016/j.jhazmat.2011.02.010

Nomenclature

Notations

C_μ, $C_{1\varepsilon}$, $C_{2\varepsilon}$	k–ε model parameters: 0.09, 1.44, 1.92
C	specie concentration (ppm)
c_p	specific heat (J/(kg K))
D	mass diffusivity (m^2/s)
d_p	catalyst particle nominal diameter (m)
E	thermal energy (J)
$\vec{g}$	gravitational acceleration, 9.81 m/s^2
G	gas mass flux (kg/m^2 s)
G_{kL}	generation rate of turbulent kinetic energy
h	convective heat transfer coefficient (W/(m^2 K))
$\mathbf{I}_q$	interphase momentum exchange term
k	k–ε model kinetic energy
K	mass transfer coefficient (m/s)
k_f	thermal conductivity (W/(m K))
k_{eff}	effective thermal conductivity (W/(m K))
l	characteristic length (m)
L	liquid mass flux (kg/m^2 s)
$\hat{n}_w$	unit vector normal to the wall
Nu	Nusselt number [hl/k_f]
p	pressure (bar)
Pr	Prandtl number [$C_p\mu/k_f$]
$-r$	oxidation rate ((mg/L) × (1/min))
Re_q	Reynolds number of qth phase [$\rho_q u_q d_p/\mu_q$]
S_i	source mass for phase i (ppm)
Sh	Sherwood number [Kl/D]
S_h	source term containing volumetric reaction heat (J)
t	time (s)
$\hat{t}_w$	unit vector tangential to the wall
T	temperature (K)
TOC	total organic carbon (ppm)
$\vec{u}$	superficial vector velocity (m/s)
z	axial coordinate (m)

Greek letters

α_i	volume fraction of ith phase
ε	k–ε model dissipation energy
κ	gas–liquid interface curvature
ρ_q	density of qth phase (kg/m^3)
Δp	total pressure drop (Pa)
σ	surface tension coefficient
σ_k, σ_ε	k–ε model parameters: 1.2, 1.0
τ	residence time (s)
$\overline{\overline{\tau_q}}$	viscous stress tensor of qth phase (Pa)
$\overline{\overline{\tau_{t,q}}}$	turbulent stress tensor of qth phase (Pa)
θ_w	contact angle at the wall
μ_q	viscosity of qth phase (Pa s)

Subscripts

G	gas phase
q	qth phase
L	liquid phase
n, m	Cartesian coordinate direction
S	solid phase

Then, the application of CFD is reinforced by its investigation on the minimization of hazardous materials.

Iliuta et al. investigated how plugging affect hydrotreating performance by simulating simultaneous fines deposition under catalytic in hydrodesulfurization in TBRs [7]. The three-phase heterogeneous model developed to simulate the trickle bed performance incorporates the concentration gradients inside the catalyst particle and solid deposit. The model correctly handled the effect of the fine particles deposition process being identified the bed plugging and the increase of the resistance to two-phase flow. Ayude et al. presented a phenomenological approach to interpret the effect of liquid flow modulation in TBRs at the particle scale [8]. Dynamic reactant profiles inside the catalytic particle were obtained for different cycling and system conditions being the experimental trends explained with this approach. Liu et al. examined the periodically operated TBR for ethylanthraquinones hydrogenation [9]. A dynamic model was verified by simulating the effect of cycle period and split on the conversion and the selectivity enhancement and compared with the experimental results. An experimental and theoretical study of forced unsteady-state operation of TBR was presented by Lange et al. in comparison to the steady-state operation. The simulation studies demonstrate that the liquid flow variation has a strong influence on the liquid hold-up oscillation and on the catalyst wetting efficiency [10]. Rajashekharam et al. developed a TBR model for the hydrogenation of 2,4 dinitrotoluene with experimental verification [11]. The model incorporates the contributions of partial wetting and stagnant liquid hold-up effects in addition to external and intraparticle mass transfer resistances for a complex consecutive/parallel reaction scheme under consideration represented by Langmuir–Hinshelwood kinetics.

On the investigation of CFD for the risk assessments related to industrial environments, Calay and Holdo have modelled the dispersion of flashing jets in where gas is kept in liquid form under high-pressure [12]. The authors presented reproducible results to those phenomena related to turbulence, droplet transport, evaporation, break-up and coalescence events. Gavelli et al. presented a reliable method to quantify and bound LNG vapour dispersion hazard distances for regulatory purposes [13]. The mathematical models encompass conservative assumptions in the derivation of the LNG vapour source term. It is suggested that sophisticated models could be used to predict the flow and vaporization of LNG by numerical integration of the shallow water equations. Pontiggia et al. have assessed the consequences of hazardous gas releases in urban areas through CFD simulations [14]. Once again, CFD has demonstrated its versatility to represent realistically such complex geometries in detailed simulation models leading to three-dimensional flow fields that strongly influence gas dispersion. The authors have pointed out that integral models can both overestimate and underestimate the magnitude of consequences related to hazardous material releases in urban areas.

From the above survey, CFD models can be trustfully applied in different frameworks, nevertheless such approach has scarcely been reported to predict the reaction behaviour of trickle beds. Apart from the hydrodynamic models evolved at cold flow conditions, we extend our previous VOF model to gain further insight on how process parameters such as liquid velocity, surface tension and wetting phenomena affect the multiphase flow in high-pressure trickle-bed reactor. A Volume-of-Fluid model was developed to simulate the multiphase reactive flow in the catalytic wet oxidation of mimicked agro-industry effluents. As long as the temperature and liquid flow rate play a major role on the decontamination rate of liquid pollutants, several computational runs have to be validated accordingly and performed under transient conditions. This methodology provides a more fundamental understanding of flow environment and TBR chemical behaviour.

2. Mathematical model

2.1. Governing flow equations

A trickle bed based on a cylindrical geometry (50 mm_{ID} × 1.0 m_{Length}) was modelled with a specified void fraction and a

set of fluid physical properties. The computational geometry was designed so that a distance gap of about 3% of the sphere diameter facilitates the grid generation avoiding numerical difficulties that arise in the calculation of convective terms as described elsewhere [15,16]. The VOF method was used to compute velocity field, liquid volume fraction distributions as well as the total organic carbon concentration that was used to quantify the mineralization degree of liquid pollutants. The multiphase flow is assumed to be vertical downward and incompressible, with the mathematical description based on the Navier–Stokes equations for momentum and mass conservation of a viscous fluid flow through a three-dimensional catalytic bed. The variable fields are shared by both phases and correspond to volume-averaged values knowing the volume fraction, α_q, of each phase, q, in the entire computational domain. The volume fraction equation for the phase q is given by:

$$\frac{\partial}{\partial t}(\alpha_q \rho_q) + \nabla \cdot (\alpha_q \rho_q \mathbf{U}_q) = 0, \quad \text{with} \quad q = g \quad \text{or} \quad l \tag{1}$$

where g and l denote, respectively, the gas and liquid phases, t, being the time, and through the resolution of the momentum equation shared by the two considered fluids:

$$\frac{\partial}{\partial t}(\alpha_q \rho_q \mathbf{U}_q) + \nabla \cdot (\alpha_q \rho_q \mathbf{U}_q \mathbf{U}_q) = -\alpha_q \nabla p + \alpha_q \rho_q \mathbf{g} + \nabla \cdot \alpha_q \left(\overline{\overline{\tau_q}} + \overline{\overline{\tau_{t,q}}}\right) + \mathbf{I}_q, \quad \text{with} \quad q = g \quad \text{or} \quad l \tag{2}$$

where p, $\mathbf{g}$ and the physical properties (density, ρ; and viscosity, μ) being determined by volume-weighted averages. $\mathbf{I}_q$ is the interphase momentum exchange term and $\overline{\overline{\tau_q}}$ and $\overline{\overline{\tau_{t,q}}}$ are, respectively, the viscous stress tensor and the turbulent stress tensor, defined as follows:

$$\overline{\overline{\tau_q}} = \mu_q (\nabla \mathbf{U}_q + \nabla \mathbf{U}_q^t) + \left(\lambda_q - \frac{2}{3}\mu_q\right) \nabla \mathbf{U}_q \bar{\bar{I}} \tag{3}$$

and

$$\overline{\overline{\tau_{t,q}}} = \mu_{t,q} (\nabla \mathbf{U}_q + \nabla \mathbf{U}_q^t) - \frac{2}{3}(k_q + \mu_{t,q} \nabla \mathbf{U}_q) \bar{\bar{I}} \tag{4}$$

2.2. Free surface model: surface tension and wall adhesion

The continuum surface force model proposed by Brackbill et al. has been used to compute the surface tension [17]. The pressure drop across the surface depends upon the surface tension coefficient, σ, and the surface curvature as measured by two radii in orthogonal directions, R_1 and R_2, as expressed in Eq. (5):

$$p_2 - p_1 = \sigma \left(\frac{1}{R_1} + \frac{1}{R_2}\right) \tag{5}$$

where p_1 and p_2 are the pressures in the two fluids on either side of the interface. The surface curvature is computed from local gradients in the surface normal at the interface. n is the surface normal, defined as the gradient of α_i : $n = \nabla \alpha_i$. The curvature, κ, is defined in terms of the divergence of the unit normal, $\hat{n}$: $\kappa = \nabla \cdot \hat{n}$ where $\hat{n} = n/|n|$. The forces at the surface are expressed as a volume force using the divergence theorem assuming the form of Eq. (6):

$$F_j = \sum_{pairs\ ij, i<j} \sigma_{ij} \frac{\alpha_i \rho_i \kappa_j \nabla \alpha_j + \alpha_j \rho_j \kappa_i \nabla \alpha_i}{1/2(\rho_i + \rho_j)} \tag{6}$$

2.3. Species continuity and energy equations

The predicted flow field including velocities and volume fractions of both phases was further used to solve species transport equations in the catalytic wet air oxidation of a model phenolic solution in the trickle-bed reactor. These equations are expressed in the mass balance equation for any species, i:

$$\frac{\partial \alpha_q \rho_q C_{q,i}}{\partial t} + \nabla \cdot (\alpha_q \rho_q u_q C_{q,i}) = \nabla \cdot (\alpha_q \rho_q D_{i,m} \nabla C_{q,i}) + \alpha_q \rho_q S_{q,i} \tag{7}$$

where $C_{q,i}$ is the concentration of species i in the qth phase (gas or liquid), ρ_q and α_q is the density and volume fraction of the qth phase. $S_{q,i}$ is the source for species i in phase q. Volume averaged properties of fluids were used for calculating the flux across the control cell. Two-film theory was used for accounting mass transfer and the resistance in gas–liquid film was considered as the rate limiting resistance [18]. Mass transfer coefficient was computed according to the Satterfield et al. correlation and heat transfer coefficient was calculated according to the correlation developed by Boelhouwer et al. as expressed in Eqs. (8) and (9), respectively [19,20].

$$Sh = 0.815 Re^{0.822} Sc^{1/3} \tag{8}$$

$$Nu = 0.111 Re^{0.8} Pr^{1/3} \tag{9}$$

The energy equation, also shared among the phases, is shown in Eq. (10):

$$\frac{\partial}{\partial t}(\rho E) + \nabla \cdot (\vec{v}(\rho E + p)) = \nabla \cdot (k_{eff} \nabla T) + S_h \tag{10}$$

The VOF model treats energy, E, and temperature, T, as mass-averaged variables:

$$E = \frac{\sum_{q=1}^{n} \alpha_q \rho_q E_q}{\sum_{q=1}^{n} \alpha_q \rho_q} \tag{11}$$

where E_q for each phase is based on the specific heat of that phase and the shared temperature.

The properties ρ and k_{eff} (effective thermal conductivity) are shared by the phases. The source term, S_h, contains contributions from volumetric reaction heat sources, which is given by the product $\Delta H \times \rho \times r_{TOC}$.

2.4. Two-phase k–ε turbulence model

Taking into account that the Reynolds numbers range for the gas phase is wide (min: 10, max: 2500), the mixture k–ε approach is used for turbulence modelling [21]. For incompressible flows, the turbulence parameters are calculated from Eqs. (10) and (11):

$$\frac{\partial}{\partial t}(\rho_m k) + \nabla \cdot (\rho_m \vec{u}_m k) = \nabla \cdot \left(\frac{\mu_{t,m}}{\sigma_k} \nabla k\right) + G_{k,m} - \rho_m \varepsilon \tag{12}$$

$$\frac{\partial}{\partial t}(\rho_m \varepsilon) + \nabla \cdot (\rho_m \vec{u}_m \varepsilon) = \nabla \cdot \left(\frac{\mu_{t,m}}{\sigma_\varepsilon} \nabla \varepsilon\right) + \frac{\varepsilon_m}{k_m} \times (C_{1\varepsilon} G_{k,m} - C_{2\varepsilon} \rho_m \varepsilon) \tag{13}$$

and the turbulent viscosity $\mu_{t,m}$ and the production of turbulence kinetic energy, $G_{k,m}$ are computed from Eq. (14):

$$\mu_{t,q} = \rho_q C_\mu \frac{k_q^2}{\varepsilon_q}$$

$$G_{k,m} = \mu_{t,m} (\nabla \vec{u}_m + (\nabla \vec{u}_m)^T) : \nabla \vec{u}_m \tag{14}$$

C_μ is equal to 0.09 and $C_{1\varepsilon}$ and $C_{2\varepsilon}$ are the constants of standard k–ε model: 1.44 and 1.92, respectively, whereas σ_k and σ_ε are the turbulent Prandtl numbers for k and ε, 1.0 and 1.3, respectively.

2.5. Numerical simulation

The interstitial space of the trickle-bed reactor was designed through a tetrahedral mesh, which was created using the integrated

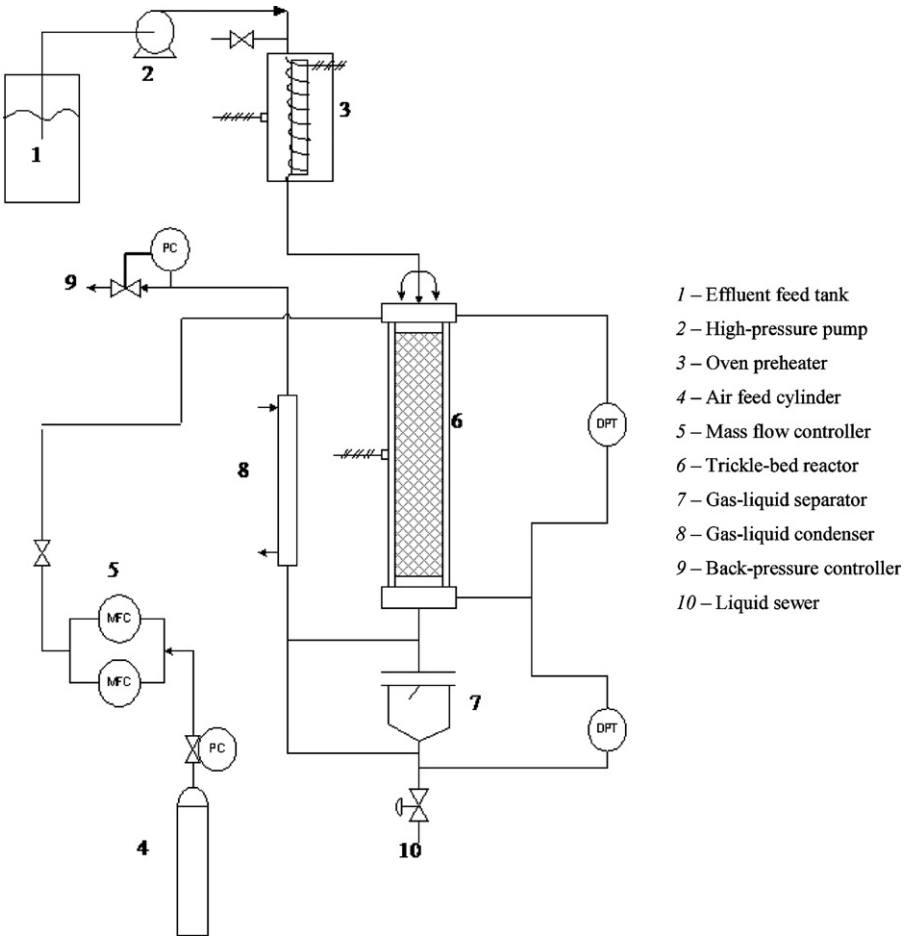

Fig. 1. Schematic diagram of trickle-bed reactor experimental set-up.

solid modelling and meshing program GAMBIT [22] mimicking the characteristic dimensions of commercial catalyst N-140 supplied by the Süd-Chemie Group, Munich. The VOF method simulates free-surface flow by means of a fluid fraction function, which has a value between unity and zero. The discretization of the governing equations is done by the finite-volume method. The grid independency was established after the evaluation of different mesh natures and apertures in order to isolate mesh related discretization errors. All transport equations were discretized to be at least second order accurate in space. A segregated implicit solver available in commercial CFD package FLUENT 6 [23] was employed to evaluate the resulting linear system of equations. The conditions required for grid convergent results are based on a 1% relative error criterion and the simulations accuracy has been assessed by comparisons to experimental data available in the literature. At the interface, the additional interaction conditions depend on interfacial velocity and gradient of the surface tension.

The CWAO kinetic parameters for the commercial catalyst N-140 were similarly derived to the work developed by Lopes et al. [24]. The right-hand side term of Eq. (7), $S_{i,q}$, include the reaction rates in terms of the total organic carbon concentration of the lumped species *A*, *B* and *C* as represented in Eq. (15):

$$-r_{\mathrm{TOC}_A} = -\frac{dC_{\mathrm{TOC}_A}}{dt} = (k'_1 + k'_2)C_{\mathrm{TOC}_A}$$
$$-r_{\mathrm{TOC}_B} = -\frac{dC_{\mathrm{TOC}_B}}{dt} = k'_3 C_{\mathrm{TOC}_B} - k'_2 C_{\mathrm{TOC}_A} \quad (15)$$

where first order reactions were assumed for each mechanism step of the Generalized Kinetic Model. GKM considers three types of compounds: easier degraded reactants (*A*); intermediates with difficult degradation (*B*) and desired end products, namely carbon dioxide and water (*C*). In the oxidation process of the phenolic solutions with N-140 catalyst, phenol and acetic acid were formed as intermediate compounds, being totally degraded during the treatment and the overall TOC practically reduced to zero. After integrating these equations a mathematical expression for TOC evolution is obtained in Eq. (16):

$$\frac{C_{\mathrm{TOC}}}{C_{\mathrm{TOC}_0}} = \frac{k'_2}{k'_1 + k'_2 - k'_3} e^{-k'_3 t} + \frac{k'_1 - k'_3}{k'_1 + k'_2 - k'_3} e^{-(k'_1 + k'_2)t} \quad (16)$$

The activation energies and the pre-exponential factors were calculated by using the Arrhenius plot for the N-140 kinetic studies. These values were used in the corresponding expressions of the reaction rate constants k'_1, k'_2, k'_3 as a function of temperature, according to Arrhenius law as described in Eq. (17):

$$k'_1 = 452 \cdot \exp\left(-\frac{3.121 \times 10^3}{T}\right) \ \mathrm{min}^{-1};$$
$$k'_2 = 28.1 \cdot \exp\left(-\frac{3.612 \times 10^3}{T}\right) \ \mathrm{min}^{-1}; \quad (17)$$
$$k'_3 = 4.32 \times 10^6 \cdot \exp\left(-\frac{9.814 \times 10^3}{T}\right) \ \mathrm{min}^{-1}$$

The trickle-bed reactor studies have been carried out in pilot plant as illustrated in Fig. 1 comprising a cylindrical reactor in stainless steel (SS-316) with 50 mm of internal diameter and 1.0 m length and the experimental procedure has been described elsewhere [25].

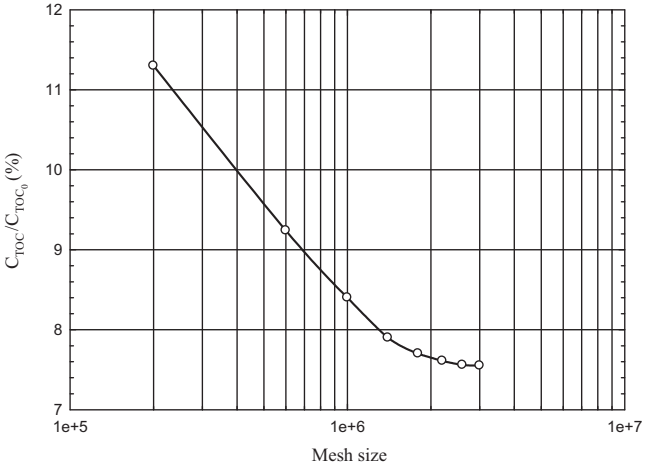

Fig. 2. Comparison of CFD predictions on normalized total organic carbon concentration for different mesh resolutions ($L = 6$ kg/m^2 s, $G = 0.3$ kg/m^2 s, $P = 30$ bar, $d_p = 2$ mm).

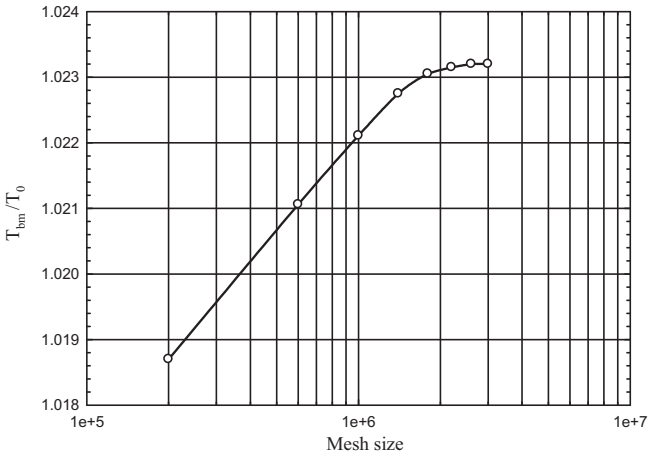

Fig. 3. Comparison of CFD predictions on normalized bulk temperature for different mesh resolutions ($L = 6$ kg/m^2 s, $G = 0.3$ kg/m^2 s, $P = 30$ bar, $d_p = 2$ mm).

3. Results and discussion

3.1. Mesh and time sensitivity tests

To check grid independence, several computational runs were carried out to figure out the mesh density with different apertures. An introductory parametric optimization was also accomplished querying the effect of different differencing schemes on the momentum and volume fraction balance equations. High-order differencing schemes based on Compressive Interface Capturing Scheme for Arbitrary Meshes (CICSAM) and High Resolution Interface Capturing (HRIC) schemes were found to agree better with the experimental data from the literature given that its formulation includes inherently the minimization of artificial numerical dissipation as described elsewhere [6].

We begin with a base case querying the influence of numerical solution parameters including different mesh apertures. The refinement is performed in eight levels: four levels for the coarser meshes with 2×10^5, 6×10^5, 1×10^6, 1.4×10^6 of tetrahedral cells and four levels for the finer meshes with 1.8×10^6, 2.2×10^6, 2.6×10^6 and 3×10^6 of tetrahedral cells. Fig. 2 displays the influence of the number of tetrahedral cells on the total organic carbon concentration profile when the catalytic abatement of phenolic wastewaters was simulated at $L = 6$ kg/m^2 s, $G = 0.3$ kg/m^2 s and $T = 200\,^\circ$C, $P = 30$ bar. As can be seen from Fig. 2, the increase of mesh density led to an asymptotic solution as one increases the number of cells from 2.2×10^6 onwards. Low mesh density characterized by 2×10^5 of tetrahedral cells at particle surface led to erroneous solutions due to an incorrect definition of boundary layer. As long as the mesh density increases, the theoretical predictions of total organic carbon conversion improve noticeably. Concerning the mesh sensitivity analysis, several computational runs were additionally performed changing the mesh density in the catalyst particle surface to properly capture the boundary layer now on the temperature profile. The effect of mesh aperture on the thermal behaviour of the trickle-bed reactor is portrayed in Fig. 3 at $L = 6$ kg/m^2 s, $G = 0.3$ kg/m^2 s and $T = 200\,^\circ$C, $P = 30$ bar. Once again, the CFD predictions converged as soon as we used a computational grid comprising 2.2 million of tetrahedral cells. Another mathematical output information revealed in Figs. 2 and 3 is related to the monotony of the total organic carbon conversion and temperature profiles. As evidenced by the mesh sensitivity analysis, the asymptotic demeanour of total organic carbon profile is monotonically decreasing until the final conversion approaches the experimental value at steady-state. On the contrary, the temperature profile is a monotonically decreasing function as one increases the density of the computational grid. Provided that the catalytic wet oxidation follows the Arrhenius's law, the higher conversions or lower percentages of the ratio C_{TOC}/C_{TOC_0} are accompanied with increasing values of the bulk phase temperature, see Fig. 3.

The numerical integration encompassed by the CFD model is also dominated by the time-stepping methodology. In the CFD multiphase calculations, we employed first-order and second-order time discretization methods. This latter scheme was found to give confident computed results in comparison to the former one as long as the second-order time-accurate scheme achieves its accuracy by using an Euler backward approximation in time. This fact can in all likelihood be ascribed to the fully implicit methodology which highlighted an unconditional stability. A fair implementation of one of these methods for solving the scalar transport equation entails more than the time-stepping formula. Additionally, we have investigated the time step in the range: 10^{-5}, 10^{-4}, 10^{-3} and 10^{-2} s. Fig. 4 plots the CFD computations of total organic carbon conversions attained with those values at $L = 6$ kg/m^2 s, $G = 0.3$ kg/m^2 s and $T = 200\,^\circ$C, $P = 30$ bar. A similar asymptotic trend was depicted in Fig. 4 so we have identified a time step of 10^{-5} s which agreed better with the experimental data. Concomitantly, the analysis of the temperature profile obtained at $L = 6$ kg/m^2 s, $G = 0.3$ kg/m^2 s and $T = 200\,^\circ$C, $P = 30$ bar reinforced the above-mentioned selection on

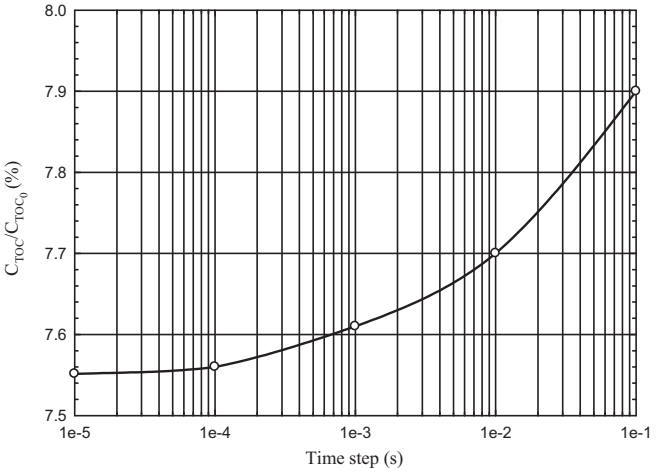

Fig. 4. Effect of time step on normalized total organic carbon concentration ($L = 6$ kg/m^2 s, $G = 0.3$ kg/m^2 s, $P = 30$ bar, $d_p = 2$ mm).

the time step assessment, see Fig. 5. It is worthy to notice the reverse behaviour that featured the total organic carbon concentration and temperature profiles illustrated in Figs. 4 and 5. As discussed earlier on the monotonic nature of mesh density functions, this suggests again the Arrhenius's temperature dependence of the rate constant for the chemical oxidation reaction.

3.2. Effect of temperature

At $L = 2\ kg/m^2\ s$, $G = 0.3\ kg/m^2\ s$, $P = 30$ bar, the VOF computations of total organic carbon conversion along the axial coordinate of trickle-bed reactor are shown with experimental data at different temperatures in Fig. 6. In the range 160–200 °C, five characteristic temperatures of catalytic wet oxidation have been used to query the effect of this reaction parameter on organic matter decontamination. As expected, conversion is favoured by increasing the temperature, hence we have the complete mineralization of organic matter after one half of reactor length when the simulation was carried out at the highest temperature (200 °C), see Fig. 6e. However, none experimental measure on total organic carbon concentration has indicated that we have an absolute depletion of organic pollutants from the liquid phase. Examination of successive plots of Fig. 6, provides the ability to compare quantitatively

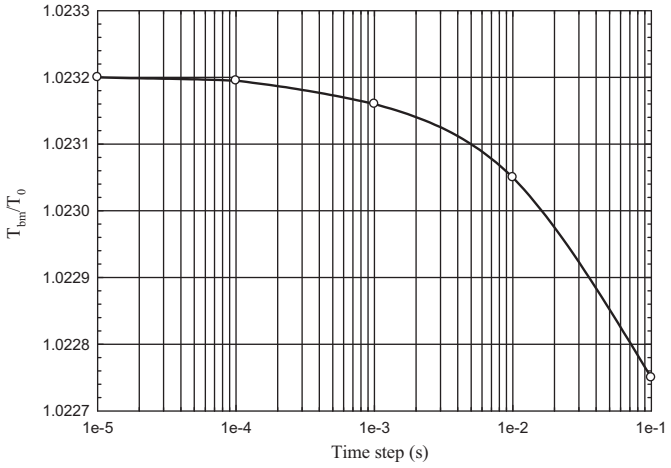

Fig. 5. Effect of time step on normalized bulk temperature ($L = 6\ kg/m^2\ s$, $G = 0.3\ kg/m^2\ s$, $P = 30$ bar, $d_p = 2$ mm).

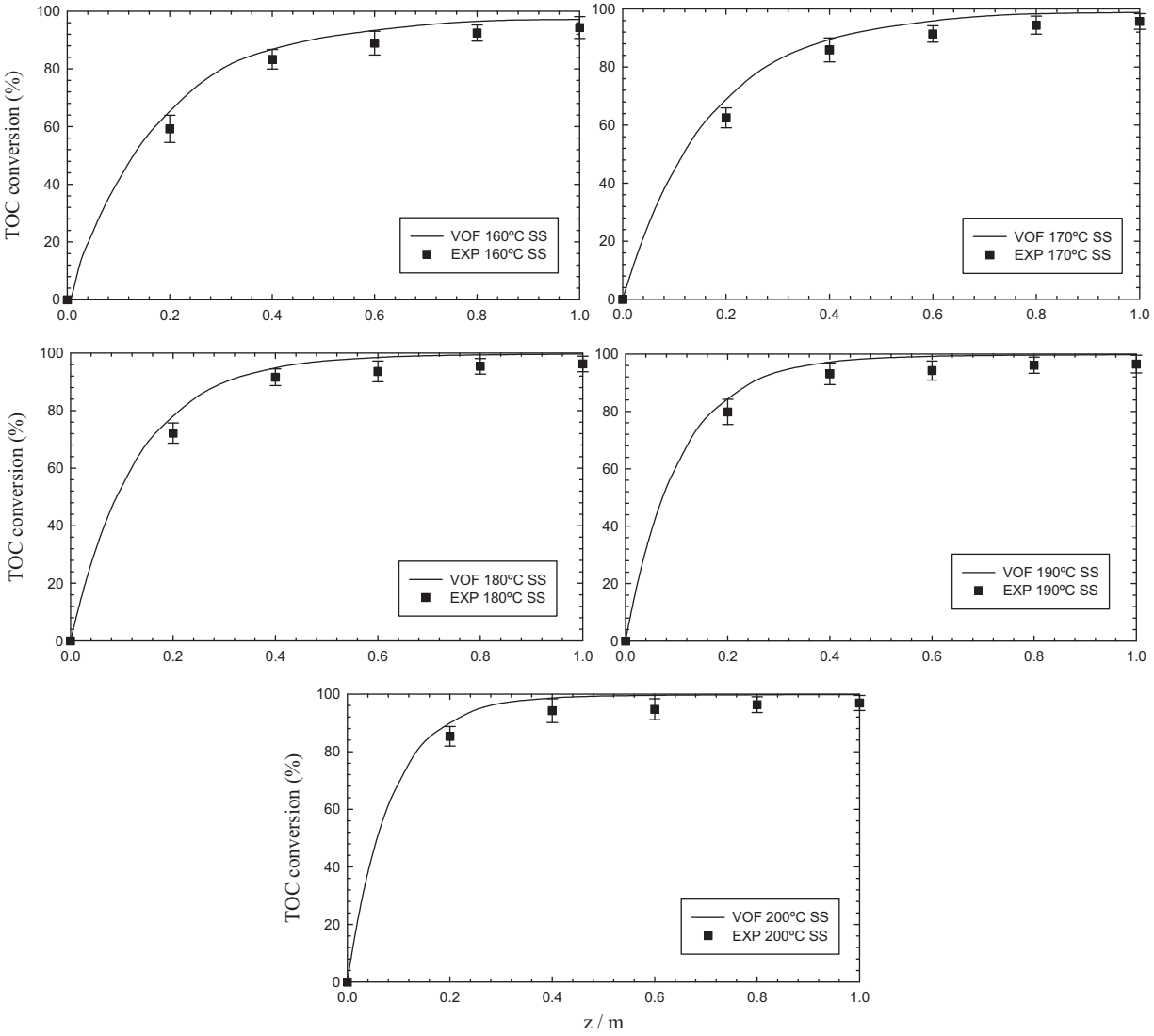

Fig. 6. Mean bulk total organic carbon conversion profiles for axial coordinate at different temperatures ($L = 2\ kg/m^2\ s$, $G = 0.3\ kg/m^2\ s$, $P = 30$ bar, $d_p = 2$ mm).

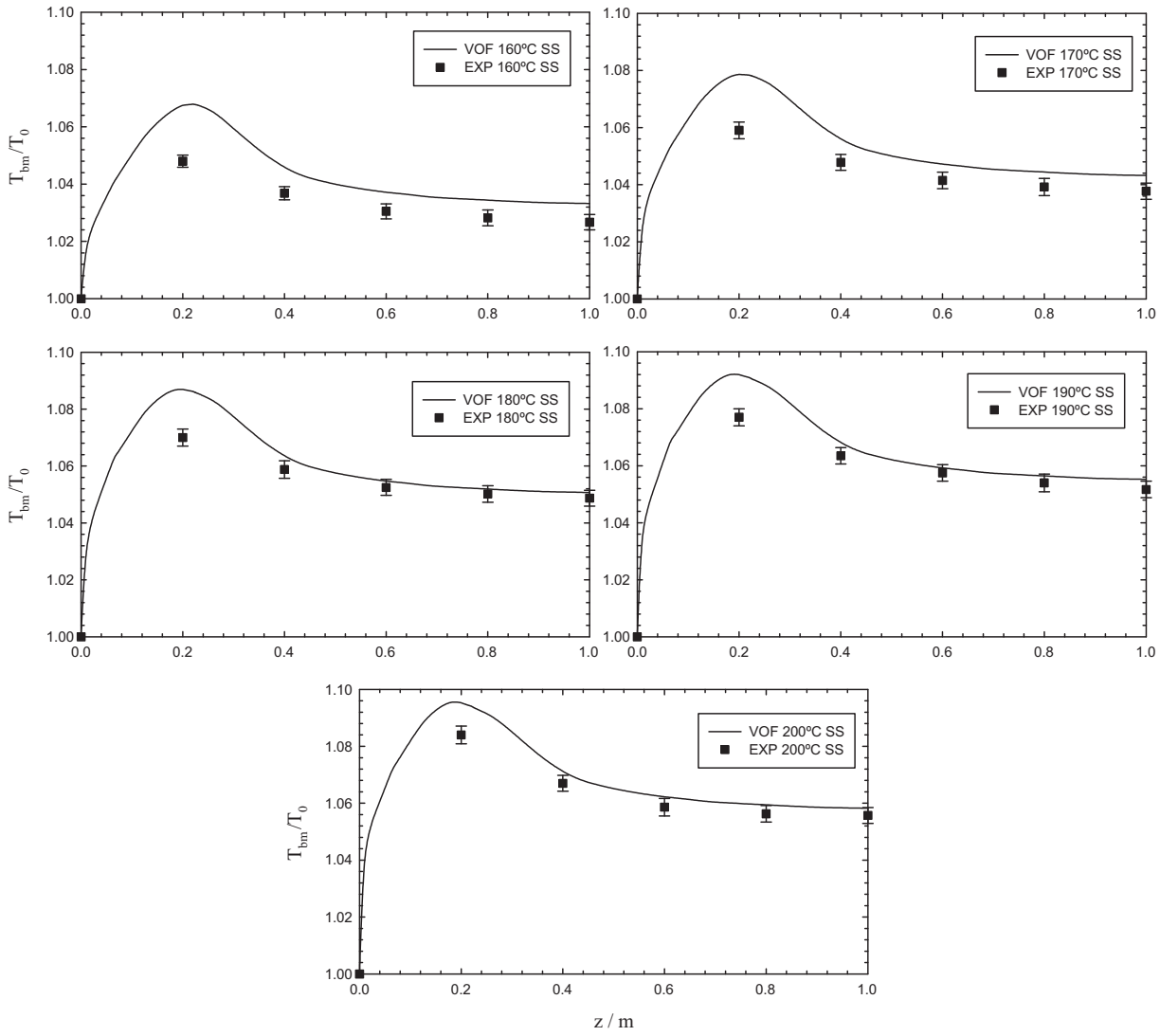

Fig. 7. Mean bulk temperature profiles for axial coordinate at different temperatures ($L = 2\ kg/m^2\ s$, $G = 0.3\ kg/m^2\ s$, $P = 30\ bar$, $d_p = 2\ mm$).

CFD model predictions with the corresponding experimental conversion either through the averaged relative or absolute errors. At the lowest temperature ($T = 160\ ^\circ C$, see Fig. 6a), the averaged relative errors obtained at $z = 0.2$, 0.4, 0.6, 0.8 and 1 m were 16.2, 24.6, 43.1, 46.4 and 44.8%, respectively. Despite these values are remarkably increasing, the averaged absolute errors are decreasing and we had achieved 5.9, 3.6, 3.8, 2.9, and 2.1 for $z = 0.2$, 0.4, 0.6, and 0.8, 1 m, respectively. In fact, the magnitude of the relative errors can be explained by the narrow range of TOC concentrations that were obtained at the reactor egress. At $z = 0.6$ and 0.8 m the TOC conversions were higher than 90% which produced very low concentration ratios C_{TOC}/C_{TOC_0} as illustrated in Fig. 6. This behaviour on the complementary nature of both averaged relative and absolute errors warned that every validation accomplished with VOF multiphase model should follow a systematic comparison between those rating parameters. Indeed, at $T = 170\ ^\circ C$ the averaged relative errors obtained with CFD model were 18.6, 30.6, 57.8, 64.1 and 65.9% for $z = 0.2$, 0.4, 0.6, 0.8 and 1 m whereas the averaged absolute errors were 6.4, 3.8, 4.1, 2.9, and 2.1, respectively. Moreover, at the highest temperature the magnitude of the averaged relative errors was enlarged hastily to 32.5, 78.4, 90.6, 90.9 and 91.4% albeit the averaged absolute errors kept almost the same intensity that was early identified at lower temperatures as 4.1, 3.9, 3.8, 2.9 and 2.4 for $z = 0.2$, 0.4, 0.6, 0.8 and 1 m, respectively.

According to all VOF computations that have been carried out at $L = 2\ kg/m^2\ s$, $G = 0.3\ kg/m^2\ s$, $P = 30\ bar$, one was able to identify the recurring overestimation of total organic carbon conversion for every simulated temperature. Generally, it can be seen from Fig. 6 that computed results agreed better with experimental data at the lower temperatures. This fact has been explained by the formulation of enthalpy balance meaning that a separate enthalpy equation for each phase in Eulerian models is more efficient on the prediction of temperature, which is used to compute the species concentration, against the shared formulation for enthalpy and temperature variables accounted by the current VOF model.

At $L = 2\ kg/m^2\ s$, $G = 0.3\ kg/m^2\ s$, $P = 30\ bar$, the averaged axial temperature profiles are depicted in Fig. 7. The thermal behaviour exhibited by the trickle-bed reactor is a distinguishing feature of exothermic reactions. As long as the catalytic wet air oxidation of phenolic pollutants releases energy available from the lower enthalpy of reaction products in comparison to the higher enthalpy of reactants, the chemical conversion of those compounds into water and carbon dioxide is responsible by the temperature increase of bulk phase. This fact led to the heating of catalyst particles more pronounced in the first one fourth of trickle-bed length as portrayed in the thermal profiles of Fig. 7. The higher the inlet temperature was the stronger the increase of bulk phase temperature was attained at steady-state. The averaged relative errors at

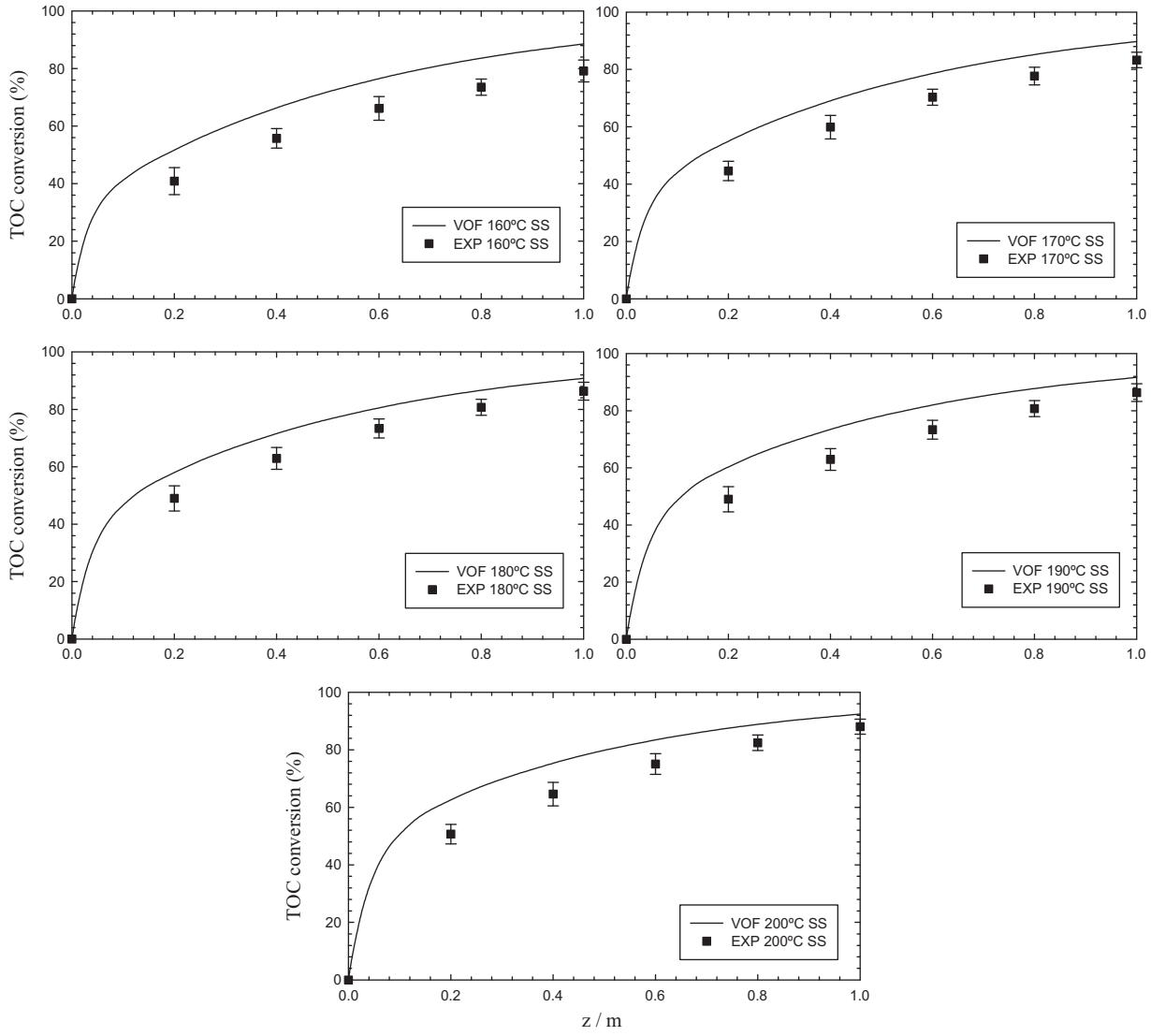

Fig. 8. Mean bulk total organic carbon conversion profiles for axial coordinate at different temperatures ($L = 6\ kg/m^2\ s$, $G = 0.3\ kg/m^2\ s$, $P = 30$ bar, $d_p = 2$ mm).

the lowest temperature were −1.7, −0.5, −0.4, −0.4 and −0.5% for $z = 0.2$, 0.4, 0.6, 0.8 and 1 m, respectively. These averaged relative errors were almost identical to the ones obtained at $T = 170\ ^\circ C$ and they have become lower when the catalytic wet oxidation was performed at the highest temperature giving −1.1, −0.5, −0.6, −0.5, and −0.3% for $z = 0.2$, 0.4, 0.6, 0.8 and 1 m, respectively. Having analysed quantitatively these findings, it can be argued that the VOF computations of total organic carbon conversion agreed better with experimental data at lower temperatures, whereas the computed VOF predictions of temperature profiles managed better at higher ones.

3.3. Effect of liquid flow rate

The VOF multiphase model has also been used to query the effect of liquid flow rate on total organic carbon conversion within the above-mentioned temperature range, 160–200 °C. Fig. 8 shows the axial profiles of total organic carbon conversion attained theoretically and experimentally at $L = 6\ kg/m^2\ s$, $G = 0.3\ kg/m^2\ s$, $P = 30$ bar. A fivefold increase on liquid flow rate led to lower decontamination rates as it can be observed from Fig. 8. This behaviour can be explained by the lower residence time of liquid phase which limited the mineralization degree expressed by reminiscent total organic carbon concentration. The maximum conversion was obtained at the highest temperature giving 90.7% while 85.1% was achieved at $T = 160\ ^\circ C$. Once again, the higher the inlet temperature is, the improved the total organic carbon conversion become at steady-state. When one increases the liquid flow rate up to $L = 6\ kg/m^2\ s$, the VOF multiphase model also overestimated the decontamination rate as already categorized at lower liquid flow rates. The five series of simulated temperatures illustrated in Fig. 8 were additionally employed on the calculation of both averaged relative and absolute errors. At the lowest temperature, the averaged relative errors attained at $z = 0.2$, 0.4, 0.6, 0.8 and 1 m were 18.2, 25.4, 32.1, 30.9 and 30.2%, whereas the averaged absolute errors were 10.1, 10.7, 10.8, 9.1 and 5.9, respectively, see Fig. 8a. Increasing the temperature up to $T = 180\ ^\circ C$, the averaged relative errors became 20.7, 27.8, 33.2, 29.6 and 23.7% while the averaged absolute errors turned out to be 10.9, 10.3, 8.7, 5.1 and 3.3 for $z = 0.2$, 0.4, 0.6, 0.8 and 1 m, respectively. If one increases even further the reactor temperature up to $T = 200\ ^\circ C$, the computed averaged relative errors were 24.7, 31.3, 35.7, 29.5 and 18.4 whereas the averaged absolute errors happened to be 11.8, 10.7, 8.8, 4.7 and 2.1, see Fig. 8e. This in return translates into an unbiased trend of deviations between the computed results and experimental data in dissimilarity with previous results obtained at the lower liquid flow rate, $L = 2\ kg/m^2\ s$, keeping

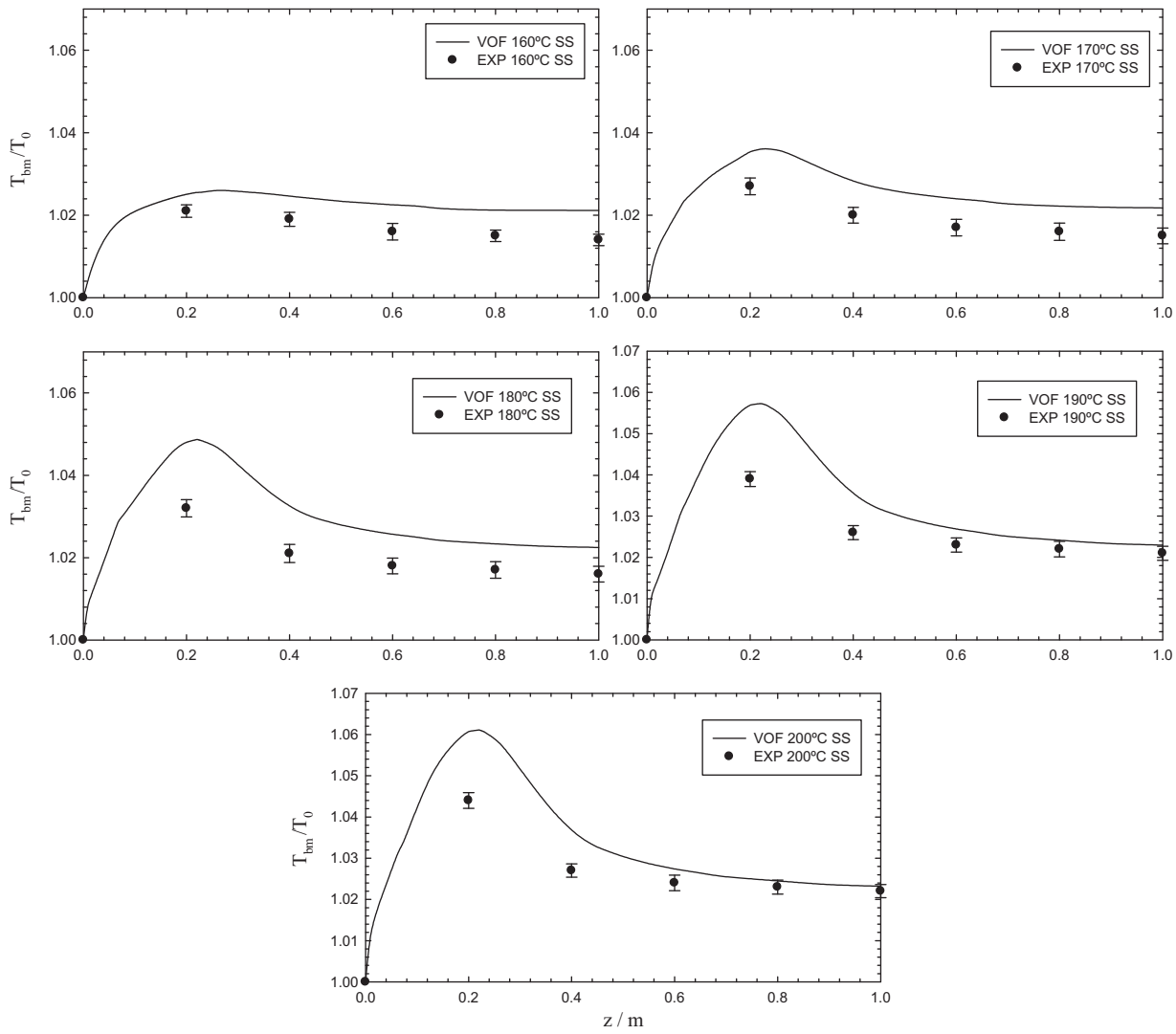

Fig. 9. Mean bulk temperature profiles for axial coordinate at different temperatures (L = 6 kg/m^2 s, G = 0.3 kg/m^2 s, P = 30 bar, d_p = 2 mm).

invariable the gas flow rate and operating pressure (G = 0.3 kg/m^2 s, P = 30 bar).

Fig. 9 shows the computed results and experimental data of the temperature profiles attained axially when the catalytic wet oxidation has been performed at the same five-valued temperature series and at L = 6 kg/m^2 s, G = 0.3 kg/m^2 s, P = 30 bar. As suggested from the simulations displayed in Fig. 9, the temperature increase predicted by the VOF multiphase model was always higher than the experimental value. As the reactor operation is now simulated at higher liquid flow rate, one should expect a reduction on the maximum temperature increase along the trickle-bed reactor. Indeed, the maximum temperature increase obtained at L = 2 kg/m^2 s was 8.9% whereas it became 5.2% at L = 6 kg/m^2 s meaning that a lower residence time did not allow for such heating degree as one observed for higher liquid phase residence time. At the lowest temperature, the averaged relative errors were −0.2, −0.3, −0.5, −0.5 and −0.6% for z = 0.2, 0.4, 0.6, 0.8 and 1 m, respectively. The magnitude of these decreased from the hotspot zone onwards with higher temperatures so we obtained −0.2, −0.1 and −0.2% for z = 0.6, 0.8 and 1 m.

3.4. Evaluation of reaction map fields

Prominent research on continuous catalytic wet oxidation of hazardous compounds has identified that hydrodynamics such as phase holdup, pressure drop, and liquid distribution are fundamental criteria for the efficient design of trickle beds. In this ambit and as long as the multiphase flow environment in trickle-bed reactors is strongly influenced by the local phase distribution and the velocity of the gas and the liquid contained in them, here we attempt to examine computationally the interstitial flow in environmentally based trickle-bed reactors given the inherent difficulties of conventional measurement methods which mainly confer a global view on the trickle bed performance.

Two representative computational mappings of interstitial flow environment are depicted in Fig. 10 at L = 6 kg/m^2 s, G = 0.3 kg/m^2 s, and P = 30 bar. This map corresponds to an instantaneous snapshot of liquid phase distribution coloured by total organic carbon concentration while Fig. 11 shows an instantaneous snapshot of liquid phase distribution coloured by temperature at the same operating conditions. The three-dimensional mappings allow us to ascertain the liquid flow consisting of rivulets and films, the former exhibiting poor liquid–solid contacting regions and the latter being good liquid–solid contacting. Indeed, this computational behaviour was experimentally observed by several authors who have systematized the rivulet/film classification in liquid distribution studies using computer-assisted tomography [26,27]. As one can observe, the liquid distribution is not uniform at the catalyst scale which identified computationally the so-called flow maldistribution of

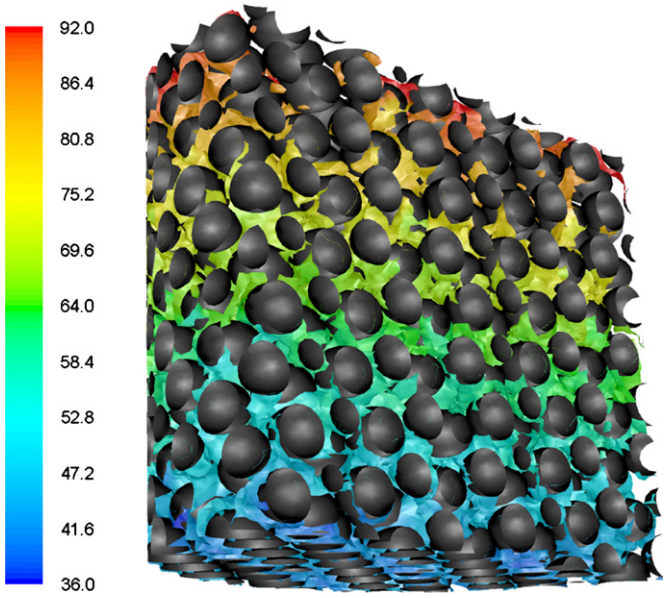

Fig. 10. Instantaneous snapshot of liquid phase distribution coloured by total organic carbon concentration ($L = 6\,kg/m^2\,s$, $G = 0.3\,kg/m^2\,s$, $P = 30\,bar$, $T = 200\,^{\circ}C$, $d_p = 2\,mm$).

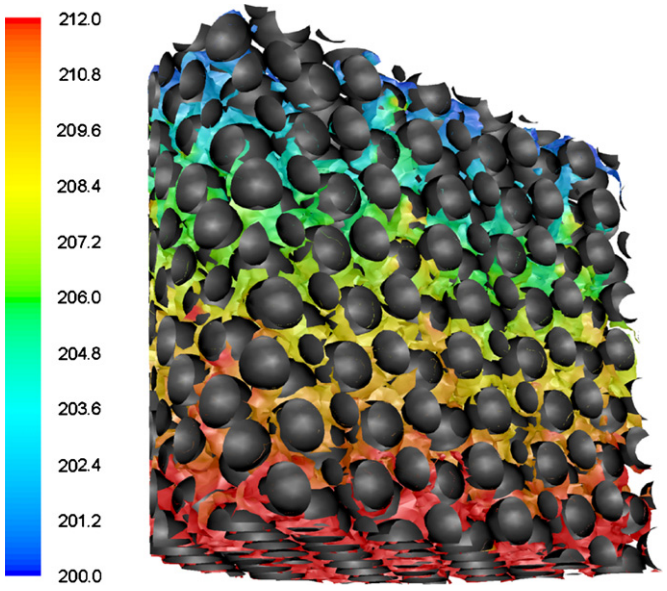

Fig. 11. Instantaneous snapshot of liquid phase distribution coloured by liquid temperature ($L = 6\,kg/m^2\,s$, $G = 0.3\,kg/m^2\,s$, $P = 30\,bar$, $T = 200\,^{\circ}C$, $d_p = 2\,mm$).

trickle beds. These strong axial and radial heterogeneities were observed experimentally by means of a magnetic resonance imaging technique to directly measure the flow in a pore space of a packed bed [28] that in turn affected the spatial distribution of reaction parameters such as the ones illustrated in Figs. 10 and 11.

4. Conclusions

Advanced CFD simulation codes can be used to intensify and demonstrate new potentialities and shortcomings in the field of modern environmental detoxification technologies. In this work, we have developed an integrated experimental and theoretical framework to give further insights into consistent, safer and cleaner remediation technology of wastewaters contaminated with hazardous compounds by catalytic wet oxidation.

First, our case study encompassed the development of a CFD multiphase model which accounts for the chemical kinetics and interphase coupling hydrodynamics in the constitutive equations. On the optimization of mesh density and time step, the CFD model correctly handled the effect of these numerical solution parameters on the computations of TOC conversion and temperature. Second, particular attention was paid to the axial profiles of temperature and TOC depletion rates. The CFD simulations have shown promising results on how fluid dynamics can be correlated with chemical reaction, namely on the prediction of total organic carbon conversions functionalized by nominal liquid flow rates and attained at different temperatures. Finally, the interstitial flow was analysed by three-dimensional computational mappings of gas–liquid distribution as well as TOC and thermal representations highlighting the inhomogeneous reactive flow environment within the trickle-bed reactor. This methodology encompassed a novel integrated tool which empowered a secure estimation of reaction properties on the simulation of hazardous and complex multiphase flows with adjustable parameters.

Acknowledgment

The authors gratefully acknowledged the financial support of *Fundação para a Ciência e Tecnologia*, Portugal.

References

[1] M.P. Dudukovic, F. Larachi, P.L. Mills, Multiphase reactors—revisited, Chem. Eng. Sci. 54 (1999) 1975–1995.
[2] J.G. Boelhouwer, H.W. Piepers, A.A.H. Drinkenburg, Advantages of forced non-steady operated trickle-bed reactors, Chem. Eng. Technol. 25 (2002) 647–650.
[3] P.L. Silveston, J. Hanika, Challenges for the periodic operation of trickle-bed catalytic reactors, Chem. Eng. Sci. 57 (2002) 3373–3385.
[4] P.L. Silveston, J. Hanika, Periodic operation of three-phase catalytic reactors, Can. J. Chem. Eng. 82 (2004) 1105–1142.
[5] M.R. Khadilkar, M.H. Al-Dahhan, M.P. Dudukovic, Multicomponent flow-transport-reaction modeling of trickle bed reactors: application to unsteady state liquid flow modulation, Ind. Eng. Chem. Res. 44 (2005) 6354–6370.
[6] R.J.G. Lopes, R.M. Quinta-Ferreira, VOF based model for multiphase flow in high-pressure trickle-bed reactor: optimization of numerical parameters, AIChE J. 55 (2009) 2920–2933.
[7] I. Iliuta, Z. Ring, F. Larachi, Simulating simultaneous fines deposition under catalytic hydrodesulfurization in hydrotreating trickle beds—does bed plugging affect HDS performance? Chem. Eng. Sci. 61 (2006) 1321–1333.
[8] M.A. Ayude, M.C. Cassanello, O.M. Martínez, P.M. Haure, Phenomenological approach to interpret the effect of liquid flow modulation in trickle bed reactors at the particle scale, Chem. Eng. Sci. 60 (2005) 6262–6269.
[9] G. Liu, Y. Duan, Y. Wang, L. Wang, Z. Mi, Periodically operated trickle-bed reactor for EAQs hydrogenation: experiments and modeling, Chem. Eng. Sci. 60 (2005) 6270–6278.
[10] R. Lange, M. Schubert, W. Dietrich, M. Grünewald, Unsteady-state operation of trickle-bed reactors, Chem. Eng. Sci. 59 (2004) 5355–5361.
[11] M.V. Rajashekharam, R. Jaganathan, R.V. Chaudhari, A trickle-bed reactor model for hydrogenation of 2,4 dinitrotoluene: experimental verification, Chem. Eng. Sci. 53 (1998) 787–805.
[12] R.K. Calay, A.E. Holdo, Modelling the dispersion of flashing jets using CFD, J. Hazard. Mater. 154 (2008) 1198–1209.
[13] F. Gavelli, M.K. Chernovsky, E. Bullister, H.K. Kytomaa, Modeling of LNG spills into trenches, J. Hazard. Mater. 180 (2010) 332–339.
[14] M. Pontiggia, M. Derudia, M. Alba, M. Scaioni, R. Rota, Hazardous gas releases in urban areas: assessment of consequences through CFD modelling, J. Hazard. Mater. 176 (2010) 589–596.
[15] R.J.G. Lopes, R.M. Quinta-Ferreira, Three-dimensional numerical simulation of pressure drop and liquid holdup for high-pressure trickle-bed reactor, Chem. Eng. J. 145 (2008) 112–120.
[16] M. Nijemeisland, A.G. Dixon, Comparison of CFD simulations to experiment for convective heat transfer in a gas–solid fixed bed, Chem. Eng. Sci. 82 (2001) 231–246.
[17] J.U. Brackbill, D.B. Kothe, C. Zemach, A continuum method for modeling surface tension, J. Comput. Phys. 100 (1992) 335–354.
[18] M. Bhaskar, G. Valavarasu, B. Sairam, K.S. Balaraman, K. Balu, Three-phase reactor model to simulate the performance of pilot-plant and industrial trickle-bed reactors sustaining hydrotreating reactions, Ind. Eng. Chem. Res. 43 (2004) 6654–6669.
[19] C.N. Satterfield, M.W. van Eek, G.S. Bliss, Liquid–solid mass transfer in packed beds with downward concurrent gas–liquid flow, AIChE J. 24 (1978) 709–717.
[20] J.G. Boelhouwer, H.W. Piepers, A.A.H. Drinkenburg, Particle-liquid heat transfer in trickle-bed reactors, Chem. Eng. Sci. 56 (2001) 1181–1187.

[21] S. Elghobashi, T. Abou-Arab, M. Rizk, A. Mostafa, Prediction of the particle-laden jet with a two-equation turbulence model, Int. J. Multiphase Flow 10 (1984) 697–710.
[22] GAMBIT 2, User's Manual to GAMBIT 2. Fluent Inc., Centrera Resource Park, 10 Cavendish Court, Lebanon, USA, 2005.
[23] FLUENT 6.1, User's Manual to FLUENT 6.1. Fluent Inc., Centrera Resource Park, 10 Cavendish Court, Lebanon, USA, 2005.
[24] R.J.G. Lopes, A.M.T. Silva, R.M. Quinta-Ferreira, Screening of catalysts and effect of temperature for kinetic degradation studies of aromatic compounds during wet oxidation, Appl. Catal. B 73 (2007) 193–202.
[25] R.J.G. Lopes, R.M. Quinta-Ferreira, Assessment of CFD Euler–Euler method for trickle-bed reactor modelling in the catalytic wet oxidation of phenolic wastewaters, Chem. Eng. J. 160 (2010) 293–301.
[26] P.G. Lutran, K.M. Ng, E.P. Delikat, Liquid distribution in trickle-beds. An experimental study using computer-assisted tomography, Ind. Eng. Chem. Res. 30 (1991) 1270–1280.
[27] P.V. Ravindra, D.P. Rao, M.S. Rao, Liquid flow texture in trickle-bed reactors: an experimental study, Ind. Eng. Chem. Res. 36 (1997) 5133.
[28] T. Suekane, Y. Yokouchi, S. Hirai, Inertial flow structures in a simple-packed bed of spheres, AIChE J. 49 (2003) 10–17.